University of BRISTOL

SCHOOL OF PHYSICS

FINAL YEAR PROJECT REPORT

NAME:	Oliver Sellers
DEGREE COURSE:	MSci Physics with Industrial Experience
PROJECT TITLE:	Pulsed Laser Deposition of Low Density Superconductors
YEAR OF SUBMISSION:	2019
SUPERVISOR:	Dr. Chris Bell
NUMBER OF WORDS:	9783

Declaration

The work in this project consisted of two distinct activities: sample growth and sample testing. The strontium titanate substrates and zirconium target were purchased from a commercial supplier. The pulsed laser deposition sample growth stage was conducted by my supervisor and myself. This started as a joint activity for the first few samples, then I was responsible for this task apart from the filling of the laser fluorine mixture. The preparation of the samples for measurement, specifically the ultra-sonic bonding of wires, was roughly equally shared between us. My share was performed under supervision. In the testing and analysis of samples, I was solely responsible for the initial testing using the dip probe once trained with the equipment. The data was logged on a LabVIEW script written by my supervisor. In the preparation for dilution refrigerator measurements, I was responsible for the design of the sample holder, which was 3D printed in the project labs. The nylon rod attachment of the sample holder to the cold plate was machined by Simon Toms (Physics Research Technician). My supervisor took charge of the cool down of the dilution refrigerator and superconducting magnet due to complexities and hazards associated with the systems and the time constraints involved. I collected and performed the analysis on the data presented in this report. Again, the collection was aided by LabVIEW scripts written by my supervisor. The two carrier fitting program was written by myself in Python using equations obtained from literature that are cited in the text.

Acknowledgements

Abstract

This project report presents the pulsed laser deposition of zirconium on strontium titanate substrates aimed at probing the crossover from conventional superconductivity (BCS theory) to the condensation of ultra-cold strongly bound diatomic Bose gases (BEC theory). Strontium titanate, in the n type doped 2D regime (2DEG), offers great potential to approach this crossover by a reduction in carrier density, due to its ability to display a bulk superconducting ground state for carrier densities many orders of magnitude lower than that of conventional metals. The results of this project show no superconducting transition for selected samples measured in a dilution refrigerator to 42 mK, the samples selected through initial resistance measurements to 5 K. This is despite strong indications from the literature that a superconducting ground state should be present. The carrier densities and mobilities, calculated from the Hall effect and magnetoresistance (MR), are comparable to normal 2DEG STO strontium titanate systems. Despite this, an interesting MR hysteresis effect was observed, suggesting magnetism present in some samples. These conclusions suggest future work should focus on understanding the lack of superconductivity, optimising the growth parameters, and exploring the possibility of magnetism in this new 2DEG system.

1   Introduction

Modern fundamental research in superconductivity primarily focuses on the limitations of the current conventional microscopic theory (BCS theory) [1]. Since its conception in 1957, many materials have been discovered that demonstrate a superconducting ground state beyond the prediction of this theory, where phonon-mediated electron pairing is unlikely. Strontium titanate is one of these materials, it displays a superconducting transition to exceptionally low carrier densities [2]. Superconductivity at such low carrier densities begins to approach a different regime, the Bose-Einstein condensate (BEC) limit, where the theory describes an ultra-cold gas of bosons. The universal pairing mechanism required for a smooth BCS-BEC crossover is currently one of the key unresolved issues in condensed matter physics [3].

Strontium titanate (STO, $SrTiO_3$) was the first discovered superconducting semiconductor with a transition temperature of a few hundred Millikelvins [4]. It is a perovskite-structured wide band gap semiconductor (3.2 eV) that can be doped either with n or p type carriers through various methods. A perovskite is characterised by the ABO_3 structure consisting of stacked layers of AO and BO_2, where A and B are cations. The dielectric constant (ε_r) of STO is the source of much interest, from 300 K to low temperatures it increases from around 300 to tens of thousands cm^2/Vs leading to low critical carrier density metal-insulator transitions [5]. Doped STO displays a finite conductivity at 0 K for carrier densities as low as 8×10^{15} cm^{-3} [6].

Conventional metallic superconductivity, specifically in mercury, was characterised by having roughly one free electron per ion, corresponding to a carrier density of the order $n_{3D} = 10^{23}$ cm^{-3}. Yet, the discovery of superconductivity in n type doped STO was found for a sample with a carrier density of 2.6×10^{19} cm^{-3} [4], four orders of magnitude lower. Further research into bulk STO samples has shown that a superconducting ground state is present to a carrier density as low as 5.5×10^{17} cm^{-3} [6]. This is now equivalent to less than one free electron per 100,000 ions, a ratio which cannot be explained within the phonon-moderated framework of BCS theory. Furthermore, superconductivity in zirconium doped strontium titanate has been shown to extend a superconducting transition to lower carrier densities with increasing dopant concentration [7]. Eagles was the first to suggest that such low-carrier density STO superconductivity is representative of a Bose gas in the BEC limit [8]. Recently, Eagles' arguments have been questioned

due to assumptions, such as an incorrect band structure of STO [2]; however, the BCS-BEC crossover is still of interest in low density superconductors.

Nakagawa *et al.* investigated gate controlled carrier densities in single-crystalline lithium-intercalated layered nitrides and showed that lightly doped 2D superconductors offer a new route to the BCS-BEC crossover [3]. Recent STO research has primarily centred on thin films and heterostructures, an interface of two semiconductors. This includes growing epitaxial thin films to investigate superconducting and normal-state transport properties [9, 10, 11, 12] and the study of the n type conducting interface between the two insulating oxides $LaAlO_3$ and $SrTiO_3$ (LAO/STO) [13, 14, 15, 16]. A recent paper from 2015 presents evidence for electron pairing at temperatures significantly above the superconducting transition temperature for the LAO/STO interface of single-electron transistors [17], the hallmark for the BCS-BEC crossover regime [18]. Therefore, the 2D limit, in the form of an epitaxial thin film combined with the previously described effect of zirconium doping in $SrTiO_3$, will allow the further probing of this novel crossover regime.

In this project, epitaxial thin films of zirconium doped strontium titanate were grown by pulsed laser deposition aimed at probing the BCS-BEC crossover. The intended, and achieved, effect was for the deposition of zirconium on the surface of the STO substrate to getter, removing oxygen from the thin film to release valence electrons to become available as carriers. The literature shows evidence for this previously being a successful mechanism in the Ar^+ irradiation of STO substrates [11, 19]. These 2DEG zirconium doped $SrTiO_{3-\delta}$ samples then underwent resistance measurements to 5 K. Further testing involved the use of a dilution refrigerator and a 12 T superconducting solenoid to test the low temperature resistance, magnetoresistance, and Hall effect for three selected samples. The results of this testing revealed no superconducting transition. The reason for this is still unclear, possible explanations are noise and grounding problems with the dilution refrigerator and high carrier densities, not in the desired range for the crossover regime. Despite the lack of superconductivity, a nonlinear Hall effect and a strong magnetoresistance were observed for the three samples, allowing the data to be fitted with the two carrier model. For the two with lowest carrier densities, a butterfly hysteresis effect was noted for a low-field sweep and, for the lowest carrier density sample, a low-field negative magnetoresistance was seen. This could suggest the formation of magnetic domains in some samples.

2 Detailed Background

2.1 Conventional Superconductivity

The observations that led to the development of BCS theory were the vanishing electrical resistance and the interior expulsion of an external magnetic field (Meissner effect) below some material dependent transition temperature (T_c), critical current density (J_c), and critical field (H_c for conventional metals). These observations suggest that the electrons in the material can be described by one macroscopic wave-function in this state, as 10^{23} cm^{-3} electrons all appear to be behaving coherently. The fundamental aspect of this is the formation of Cooper pairs. Cooper considered adding two electrons to a metal lattice at 0 K and he showed that, in the presence of an infinitesimally weak attractive potential, these electrons will form a bound state that is lower in energy than the individual states that would be occupied just above the Fermi level. In the simplest case, the energy is minimised for electrons pairing with opposite spin and momenta ($\mathbf{k} \uparrow$, $\mathbf{-k} \downarrow$) [20].
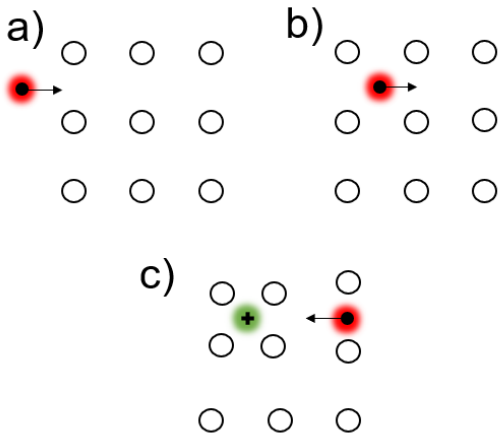

Figure 1: A diagram showing the phonon-moderated origin of the weak attractive potential in conventional metals allowing the formation of Cooper pairs. The circles represent positively charged lattice ions.

Figure 1 shows the real-space picture of the origin of this weak attraction in conventional metal superconductors. In free space, electrons experience repulsion due to their like charge but in a lattice this is reduced due to screening effects. Initially, in figure 1a), an electron close to the Fermi level moves through the lattice. At point b), the electric charge of the electron attracts the positively charged ions in the lattice. This generates a polarisation, as shown in c), which attracts the next electron with opposite momenta, acting as an attractive potential between the two electrons. Once many Cooper pairs have formed, they begin to strongly overlap to form a condensate. To break one pair would mean breaking all pairs, so an energy gap (Δ) becomes apparent between the superconducting and normal states. This means there are no scattering states available and electrical resistance vanishes. In BCS theory, the Fermi energy (ε_F) is comparable to Δ and required to be significantly larger than the energy of phonons ($\hbar\omega_D$), where $\hbar$ is the reduced Planck's constant and ω_D is the Debye frequency. The Debye frequency is a cut-off in angular frequency of the waves used to describe the motion of ions in a lattice in the Debye model, representative of the phonon frequency. Additionally, phonon-moderated superconductivity requires strong electron-phonon interactions which cause resistance at high temperatures; therefore, conventional metal superconductors have relatively high room temperature resistance.

Using the aforementioned condition regarding the relation of electron and phonon energy, Migdal's theorem can be derived which gives a crucial condition for phonon-moderated superconductivity to occur: $\hbar\omega_D \ll \varepsilon_F$ [21]. For strontium titanate with $n_{3D} = 5.5 \times 10^{17}$ cm^{-3} corresponding to $\varepsilon_F \approx 1$ meV [6], this condition is certainly not met. It is argued that this still is not representative of a Bose-Einstein condensate as the average size of Cooper pairs, the zero-temperature Ginzburg-Landau coherence length ($\xi_{GL}(0) \approx 100$ nm), is an order of magnitude larger than the interelectron distance ($d_{ee} \approx 12$ nm). Nonetheless, this superconductor still lies beyond the phonon-moderated pairing mechanism of BCS theory.

In practice, the coherence length of a thin film superconductor can be approximated by applying an out-of-plane magnetic field and using the equation $H_{c2}^\perp = \Phi_0/2\pi\xi_{GL}^2(0)$. For unconventional (type II) superconductors, H_{c2} denotes the upper critical field and $\Phi_0 = h/2e$ is the flux quantum, where h is Planck's constant and e the elementary charge. The flux quantum is a theoretically derived quantity from the quantisation of magnetic flux vortices allowed to penetrate a type II superconductor between H_{c1} and H_{c2}. Below H_{c1} is the Meissner state and the magnetic flux is perfectly expelled from the interior of the material. Above H_{c2}, the quantity of flux vortices is such that they begin to overlap and the macroscopic superconducting state is destroyed. To find $\xi_{GL}(0)$, the zero-temperature $H_{c2}^\perp$ is used, which can be found

by a linear extrapolation to 0 K [22]. In this project, the coherence length could not be estimated due to the lack of superconductivity. The interelectron distance can be calculated from $d_{ee} = n_{3D}^{-1/3}$ [6].

2.2 The BCS-BEC Crossover

The BCS-BEC crossover is essentially moving from weakly attracted pairs of fermions to a Bose gas made of strongly bound diatomic molecules. In the case of a 2DEG in the BEC limit, the electrons will form a pair, via an attractive potential and the combined half-integer spin of each electrons results in an integer spin. These paired electrons can now be considered a Bose gas of diatomic molecules and are described by the Bose-Einstein equation shown in equation 1 [23]. In this equation, n_i represents the average number of particles in state i, ε_i is the energy of state i, μ is the chemical potential, k_B is the Boltzmann constant, and T is the temperature.

$$\langle n_i \rangle = \frac{1}{e^{(\varepsilon_i - \mu)/k_B T} - 1} \qquad (1)$$

Using Bose-Einstein statistics, it is found that the condition $\mu \leq 0$ is required for equation 1 to make sense. The chemical potential is calculated by making the number of atoms in the system consistent with μ. As $T \to 0$ the chemical potential approaches zero. Below some T_{BE}, the $\mathbf{k} = 0$ state becomes macroscopically occupied and a Bose-Einstein condensate is formed. As with BCS theory, this allows a macroscopic wavefunction to be applied to the collective condensate [23]. It is clear that the pair formation is a prerequisite for the formation of a BEC.
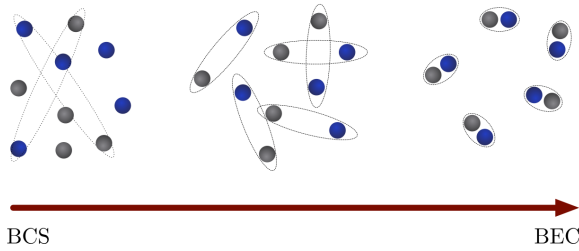

Figure 2: A diagram showing the change in pairing mechanism on the BCS-BEC crossover [23]. The different colours represent spin up and spin down electron.

Figure 2 illustrates the change in pairing mechanism as the regime moves from BCS to BEC, which is formally described in 2D by the dimensionless crossover parameter $\ln(k_F a_{2D})$. Here k_F is the Fermi wavevector and a_{2D} is the 2D scattering length. In the BCS limit, it can be seen that there is a strong overlap between the Cooper pairs that have formed for electrons with weak binding energy such that $\ln(k_F a_{2D}) \gg 1$. At the other end of the scale, where $\ln(k_F a_{2D}) \ll -1$, the size of the pairs is significantly smaller than the distance between them due to strong binding. This leads to a breaking of the global gauge symmetry of the system. The crossover regime, the middle of the scale in figure 2 where $|\ln(k_F a_{2D})| \lesssim 1$, is the region in which the Cooper pair length is roughly equal to the interelectron distance ($\xi_{GL}(0) \approx d_{ee}$). This is known as a crossover, as there is no phase transition between the two limits. In fact, it can be shown that the BCS wavefunction is formally equivalent to the BEC wavefunction but this is a derivation that is not essential to flow of discussion [24]. In the case of a 2DEG, the BCS-BEC crossover can be reached by a reduced carrier density leading to an increase in d_{ee}.

2.3 The 2-Dimensional Limit

Strontium titanate is a material that shows great promise for probing the BCS-BEC crossover in the 2DEG regime. There are several methods to perform n type doping of STO, it has most commonly been achieved by replacing Sr^{2+} ions with La^{3+} [25], replacing Ti^{4+} ions with Nb^{5+} [5], or by removing O^{2-} ions to produce reduced $SrTiO_{3-\delta}$ [6]. The latter can be initiated just by thermal lattice energy due to the relatively low binding energy and high mobility of oxygen atoms in lattice [26]. In this case, oxygen removal via zirconium deposition was performed in the 2D limit aiming to produce thin film superconductivity.

Original thought concerning superconductivity in lower dimensions raised concerns with regards to instability. Reduced screening effects from the lattice would mean that the repulsion between electrons would be stronger, reducing the probability of the formation of Cooper pairs. Additionally, it was proposed that thermal fluctuations would inhibit long range coherence between pairs. Furthermore, defects have a greater detrimental effects in lower dimensional systems. However, it now appears superconductivity in the 2D limit can be very stable indeed, with ordering temperatures and critical current densities that may significantly exceed their bulk counterparts [27]. High-quality thin film crystal structures have been produced in STO that show good superconducting stability. Kozuka *et al.*, used pulsed laser deposition to produce Nb delta-doped samples, where a thin film of Nb doped STO is grown on an insulating STO sub-

strate then sandwiched with an insulating STO sample on top [12]. The result of this was a 2D superconductor with a high-quality crystal structure capable of displaying normal state quantum oscillations, an effect described in detail in a later section.

2.4 Zirconium Doping

The selection of the method in this project is to exploit the effect witnessed by Hulm *et al.* [7], displayed in figure 3. Zirconium is a solid state solution for strontium titanate, meaning the Zr^{4+} ion can directly replace the Ti^{4+} ion.
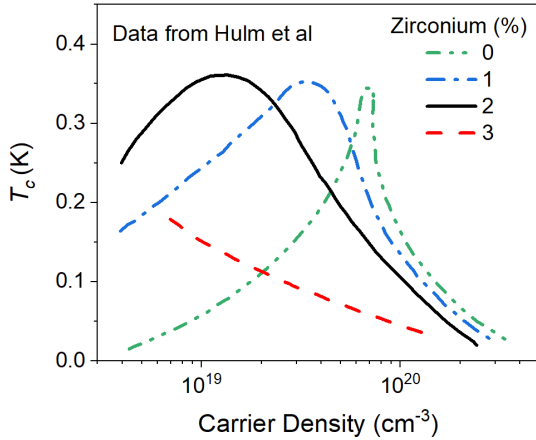

Figure 3: Data from Hulm *et al.* [7] showing the superconducting transition temperature plotted against carrier density for various quantities of zirconium doping in reduced strontium titanate.

Figure 3 presents the characteristic bell-shape curves of carrier density against transition temperature for strontium titanate. It can be seen that there is a carrier density window in which superconductivity occurs and there is a dependence of T_c on the position in this window. Schooley *et al.* [28] suggested this to be a competition between increasing density of states and carrier-carrier screening. However, this explanation relied on intervalley phonon exchange and, as shown by Lin *et al.* [6], strontium titanate's small Fermi surface has a single valley at the centre of the Brillouin zone. An alternative theory has emerged employing plasmons, a quantum plasma oscillation, for the pairing mechanism but this is not currently sufficient for higher carrier densities (10^{19} to 10^{20} cm^{-3}). Although, it is suggested that this is when electron-phonon interactions are sufficient for pairing [2].

The key aspect of figure 3 is that increasing dopant percentage leads to the superconductivity window to be translated to lower carrier densities and the width of the peak broadens. An explanation of this could be the increase in dielectric constant of the material, as seen by Alkathy *et al.* [29] in zirconium doped barium strontium titanate. The Mott criterion for critical carrier density (n_c) for a metal-insulator transition is expressed as $n_c^{1/3} a_B^* = 0.26$. It is known that a_B^* is proportional to the dielectric constant, so the increase in dielectric constant leads to a decrease in critical carrier densities [6]. Thus, metallic states can be displayed for lower carrier densities and a metallic state is a precursor to superconductivity. Additionally, it is suggested this large Bohr radius may be the reason for high electron mobilities [30]. The limit on the extent of zirconium doping that produced a superconducting transition was a result of the London penetration depth (λ). This is the length scale of the exponential decay of magnetic field at the edges of a superconductor. It was found that increasing zirconium concentration increased λ from 16 microns at 1 % to 52 microns at 3 %. The increase is said to be a result of the inability of the zirconium ion to form a mixed valence condition, leading to a hindrance in transfer of electrons from trivalent to quadravalent titantium ions. There is currently no literature reporting this effect in the 2D limit.

Although the exact concentration of zirconium will not be ascertained in this project, the carrier density will be. This is the important quantity for the interest of the BCS-BEC crossover. Quantifying the zirconium that has implanted in the system may be the focus of future work, along with adjusting growth parameters to optimise this.

3 Experimental Methods

3.1 Pulsed Laser Deposition

In figure 4, the working principles of the pulsed laser deposition can be seen. The source, a 193 nm ArF UV excimer laser, is focused on a zirconium target, rotating to avoid continuous damage to a particular region of the target. This incident radiation vaporises the zirconium, creating a diffuse plasma plume which deposits on the STO substrate surface. The intended effect is for gettering of oxygen and implantation of zirconium to occur. However, there are many mechanisms present in this pulsed laser deposition system and the growth conditions will be crucial in producing the required 2DEG samples.
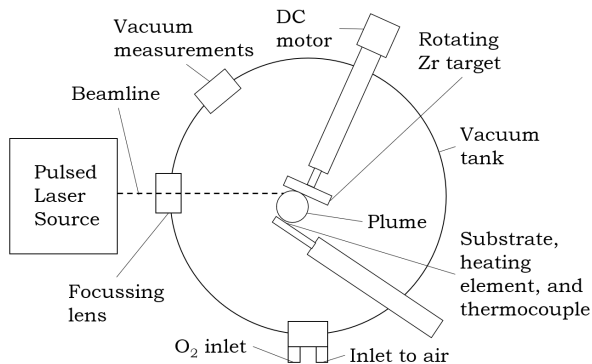

Figure 4: A schematic showing the experimental set up for sample growth through pulsed laser deposition.

The key conditions to be controlled in the growth of the samples are the substrate temperature (T_g) and the partial oxygen pressure (P_g) in the vacuum tank. The substrate temperature allows the control of the thermal energy in the STO lattice, reducing the activation energy for processes to occur. The partial oxygen pressure can have effects on the plume, such as randomising the velocity and reducing the energy of the zirconium vapour, and filling in oxygen vacancies. The substrate temperature was controlled by a heating element that the substrate samples and a type-K thermocouple were attached to with silver paint. A type-K thermocouple utilises the Seebeck effect between a Nickel-Chromium and Nickel-Alumel junction to convert voltage into temperature: this is the electromotive force caused by a temperature gradient across a two different conductive materials [31]. To control the partial oxygen pressure, first a base vacuum $(P_{base} < 10^{-6}$ mbar) was generated using a turbomolecular pump not seen in figure 4. Then flow control was used, with a Penning and a Chell vac-

uum gauge, to allow controlled volumes of oxygen gas through the O_2 inlet seen in the diagram.

The STO samples were all cut into 3×3 mm^2 pieces from the same 15×15 mm^2 SrTiO$_3$ (001) piece to ensure comparable initial surfaces across the substrates. The deposition process consisted of 5 minutes of cleaning the target with the laser at 5 Hz and 30 kV with the substrate turned away, followed by 30 minutes of deposition with the substrate facing the target at 10 Hz and 30 kV. Post-deposition, the samples were allowed to cool in the partial oxygen pressure before being removed from the vacuum chamber. Two rounds of deposition were performed, with the changing of the focusing lens between. In the first round, partial oxygen pressures of P_{base} and 10^{-4} mbar were chosen for growth temperatures of 25, 200, 400, and 600 °C. In the second round, partial pressures of 6×10^{-6} and 1.5×10^{-5} mbar were chosen for the same temperature range. The first round laser energy was calculated to be 30 mJ and the second round 55 mJ. To act as an experimental control, glass slides were deposited alongside STO substrates for growths at $T_g = 1.5 \times 10^{-5}$ mbar, the round immediately after changing the focusing lens when the laser energy was highest.

3.2 Resistance Measurements

After growth, the samples were subject to resistance measurements with temperature $(R(T))$. This was initially performed using a dip probe with a diode temperature measurement and a sample holder in a Helium-4 cryostat to reach temperatures of the order of 5 K. Aluminium wires with 1 % silicon were ultrasonically bonded to the edges of the samples. The resistance measurement was a four-point van der Pauw current biased measurement. The van der Pauw method is utilised for the square samples as it allows four-point resistance to be calculated for an arbitrary 2D shape using the equations 2 and 3, where the subscripts 1 to 4 represent a measurement at each corner [32]. R is the resistance (Ω); V is the voltage (V); I is the current (A); and R_s is the sheet resistance (Ω).

$$R_{12,34} = \frac{V_{34}}{I_{12}} \; ; \; R_{23,41} = \frac{V_{41}}{I_{23}} \qquad (2)$$

$$e^{-\frac{\pi R_{12,34}}{R_s}} + e^{-\frac{\pi R_{23,41}}{R_s}} = 1 \qquad (3)$$

The van der Pauw method assumes the sample must be flat and uniform thickness; not have any isolated holes; must be isotropic and homogeneous; the contacts must be at the edges of the sample; and the contact area must be at least an order of magnitude

smaller than the sample area. In this case, these conditions are assumed to be valid. The measurements were logged with a LabVIEW script. The current was supplied by a Keithley 220, and the voltage measured with an Agilent 34420A nano-voltmeter. The temperature was measured with a Lakeshore 336.

3.3 Low Temperature Measurements

To conduct further investigations into STO samples selected from initial $R(T)$ measurements, a dilution refrigerator was used to reach temperatures of the order 50 mK. Typical $SrTiO_{3-\delta}$ superconducting transitions are observed at a few hundreds of Millikelvins [2]; therefore, lower temperatures than 5 K were required to observe this phenomena.

The working fluid in a dilution refrigerator is a He-3/He-4. The principle of operation relies on the finite solubility of He-3 in He-4 at temperatures below 0.8 K leading to phase separation, in this case generated by the 1 K pot - an apparatus utilising evaporative cooling. Figure 5 shows the composition of the mixture for varying temperature. As the mixture is cooled, He-4 enters the superfluid phase whilst the He-3 remains a Fermi liquid. Superfluidity is a phenomenon related to Bose-Einstein condensation, in this state particles can move without dissipation, leading to fluid flow without resistance caused by viscosity. He-4 forms a superfluid as each atom has integer spin and can therefore be considered a boson. He-3 has half-integer spin atoms, so each atom must pair with another to form bosonic molecules capable of condensing; this is done via the weak attraction from the van der Waals force, so the transition temperature is significantly lower than that of He-4 (of the order mK). He-3 superfluidity is somewhat analogous to a 2DEG BEC.

It can be seen there is a forbidden region limiting the concentration of He-3 in the He-3/He-4 mixture. He-3 solubility in He-4 is a result of the interatomic bonding: the He-3 experiences stronger van der Waals forces when surrounded by He-4 atoms. This is due to the larger zero-point motion of He-3, arising from the decreased mass, so the interatomic distance is smaller for He-3 to He-4 molecules than He-3 to He-3. This leads to a favourable energy state for the He-3 to dissolve in the He-4. The limit on solubility results from the increase in Fermi energy with increasing He-3 concentration. A He-3 Fermi liquid obeys the Pauli exclusion principle, so the occupied states must increase in energy. The point at which the chemical potential of pure He-3 is equal to the Fermi energy of He-3/He-4 mixture is shown by the boundary of the forbidden region [33].
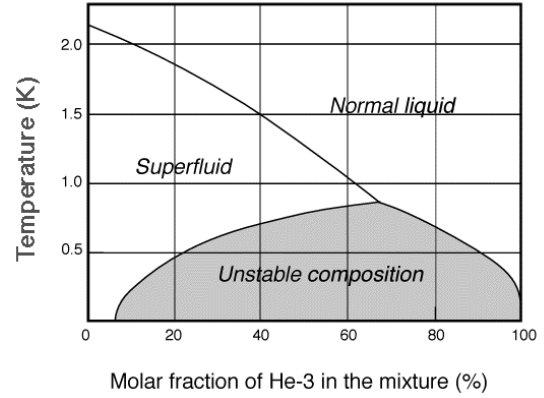

Figure 5: A plot showing the molar fraction of He-3 in He-4 for varying temperature. The normal liquid to superfluid transition is only representative of the He-4 in the mixture [34].

The cooling power is generated by removing He-3 atoms from the He-4 rich phase. When this occurs, the system will move into the favourable energy state by replenishing the removed He-3. The He-3 in the He-4 has higher enthalpy, so cooling power is generated when the He-3 moves across the boundary and dissolves. This is analogous to evaporative cooling by the 1 K pot: gaseous He-3 has higher enthalpy thus evaporation creates cooling power [33]. The dilution refrigerator allowed the $R(T)$ measurements, described in the previous section, to be extended to much lower temperatures. Again, this data was logged with a LabVIEW script. In this case the current bias was supplied by a Keithley 6220 current source and the voltage measurement taken from a Keithley 2182. The temperature measurement was performed by Oxford Instruments systems at the coldplate.

3.3.1 Hall Effect

In addition to extended $R(T)$ measurements, the 12 T superconducting magnet solenoid in the dilution refrigerator was utilised to observe the resistivity (ρ) properties in a perpendicular magnetic field ($H_{c2}^{\perp}$). When such a field is applied to a 2DEG, the off-diagonal resistivity tensor components become non-zero due to the Lorentz force $\mathbf{F} = q(\mathbf{E} + \mathbf{v} \times \mathbf{B})$ on carriers, where $\mathbf{v}$ is the velocity of the carrier, $\mathbf{B}$ is the magnetic flux density, $\mathbf{E}$ is the electric field, and q is the charge. The resistivity tensor in 2 dimensions is shown below in equation 4, where the x and y directions are in the plane of the 2DEG.

$$\underline{\underline{\rho}} = \begin{bmatrix} \rho_{xx} & \rho_{xy} \\ \rho_{yx} & \rho_{yy} \end{bmatrix} \quad (4)$$

The application of a perpendicular magnetic field results in Landau quantisation in high-field ranges. This is a quantum mechanical effect which discretises the orbits of charged particles. For electrons in a 2DEG, this is illustrated by figure 6. It can be seen that the energy landscape in **k** space is discretised into levels separated by $\hbar\omega_c$. Landau levels are degenerate and the density of states at each energy is directly proportional to the magnetic field strength. They are solely responsible for quantum oscillations, observable for high-quality crystal structures as disorder broadens Landau levels. This is where an increase in field causes the Landau levels to pass through the Fermi energy (E_F), leading to spikes in the density of states at the Fermi level. If E_F lies between two levels, the middle of the 2DEG is insulating but the edges are conducting leading to edge currents, as shown by the intersection points. When E_F lies on a Landau level, the entirety of the 2DEG becomes conducting. This change in the density of states at the Fermi level creates oscillations in the thermodynamic properties of the system. These quantum oscillations have been used previously in the literature to map the Fermi surface of STO [6]. Landau levels and edge currents are responsible for the quantum Hall effect (QHE); however, the theory of this is not relevant to the project [35].
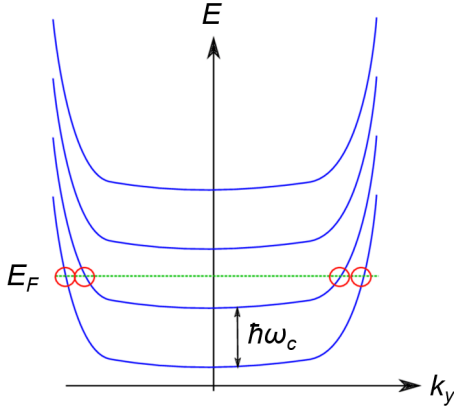
$\rho_{xy} = -\rho_{yx}$, thus simplifying the system. Due to the unknown sample thickness, the sheet resistance components R_{xx} and R_{xy} were measured by changing the configuration of the van der Pauw measurement for varying B-field. The R_{xx} component reveals the magnetoresistance of the samples and the R_{xy} components reveal the voltage induced from the Hall effect. The magnetoresistance is an even function such that $R_{xx}(B) = R_{xx}(-B)$ and the Hall resistance is an odd function such that $R_{xy}(B) = -R_{xy}(-B)$. These two measurements give insights into the conduction mechanisms of the sample and allow the calculation of the 2D sheet carrier density. The current-biased resistance measurements were logged through Lab-VIEW with the same current source and voltmeter as the previous section. The magnet power supply and measurement was provided by the Oxford Instruments system.

Figure 6: A schematic of Landau levels in a trivial 2DEG in one direction of **k** space adapted from [36]. Each level is separated by energy $\hbar\omega_c$, where ω_c represents the cyclotron frequency of orbits.

For a uniform applied field and a homogeneous and isotropic sample, $\rho_{xx} = \rho_{yy}$ and it can be shown that

4 Initial *R(T)* Measurements

4.1 Results

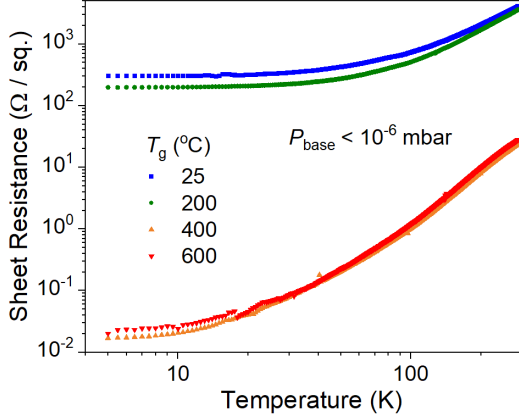The following section documents the results taken in the initial resistance measurements from 288 K to 5 K.

Figure 7: A plot showing the sheet resistance as a function of temperature for samples grown at P_{base}. The T_g values are 25, 200, 400, and 600 °C. The residual resistivity ratios (RRR) from 288 K to 5 K are 13.4, 18.1, 1403, and 1376 respectively.

In figure 7, the sheet resistance was calculated by the van der Pauw method for temperature increments interpolated from the raw four-point resistance measurements in each configuration. All the presented samples show metallic behaviour and it is clear that the general trend of decreasing sheet resistance with increasing growth temperature is followed up to 400 °C. At this point, there is no further sheet resistance decrease. In fact, a small increase is visible. A large jump in resistance between 200 and 400 °C suggests the conduction mechanisms in the samples dramatically change. The RRR values follow the reverse trend to the resistance values: increasing with increasing growth temperature up to 400 °C.

The data in figure 8 was again calculated by the van der Pauw method. The general trend is decreasing sheet resistance and increasing RRR as P_g is reduced. A slight upturn in sheet resistance at low temperatures can be observed for the $P_g = 1.5 \times 10^{-5}$ mbar sample. For the $P_g = 10^{-4}$ mbar sample, metallic behaviour is displayed at room temperature even though the sheet resistance is large. However, a clear metal to insulator transition can be seen at around 150 K.
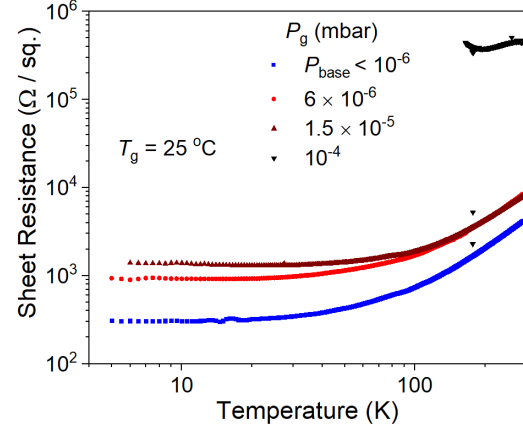

Figure 8: A plot showing the sheet resistance as a function of temperature for samples grown at $T_g = 25$ °C. The P_g values are P_{base}, 6×10^{-6}, 1.5×10^{-5}, and 10^{-4} mbar. This corresponds to RRR values of 13.4, 8.9, 5.6, and no value for $P_g = 10^{-4}$ mbar. The P_{base} data is the same as shown in figure 7.
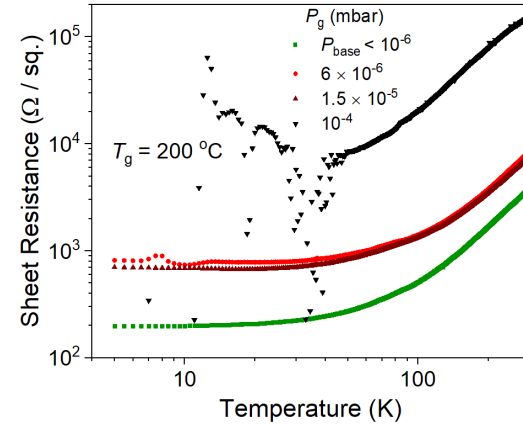

Figure 9: A plot showing the sheet resistance as a function of temperature for samples grown at $T_g = 200$ °C. The P_g values are P_{base}, 6×10^{-6}, 1.5×10^{-5}, and 10^{-4} mbar. This corresponds to RRR values of 18.1, 9.6, 10.2, and no value for $P_g = 10^{-4}$ mbar. The P_{base} data is the same as shown in figure 7.

Once more, the van der Pauw method, described previously, was used to calculate the data in figure 9. This data presents the effect that an increase in the thermal energy of the system has on growth for a range of growth pressures. It can be seen that, generally, the sheet resistance decreases for decreasing P_g. The exception being the data sets for $P_g = 6 \times 10^{-6}$ and 1.5×10^{-5} mbar, where the resistance is higher

for the former. Again, slight upturns in resistance for some data sets are visible. For the $P_g = 10^{-4}$ mbar data, a more prominent upturn is visible suggesting a metal to insulator transition. This data exhibits large quantities of noise at around 50 K, resulting from an intermittent contact problem. The data shown is the second attempt after rebonding the wires - further measurement attempts were not conducted due to time constraints.
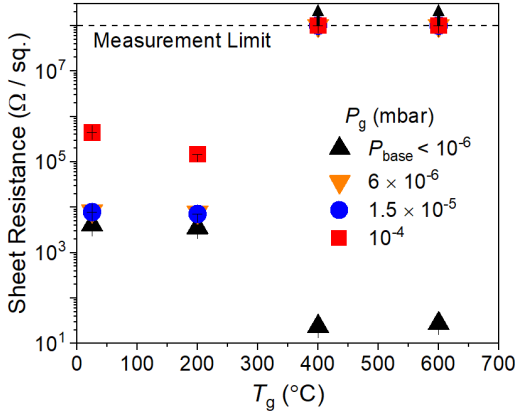

Figure 10: A plot showing the 288 K sheet resistance for each sample grown plotted against T_g. The P_g values are P_{base}, 6×10^{-6}, 1.5×10^{-5}, and 10^{-4} mbar. The dashed line represents the measurement limit of the equipment used and points on that line had immeasurable resistances.

Figure 10 gives a summary of the data presented in the previous figures with the additional insulating samples. The sheet resistance of samples with $T_g = 25$ and 200 °C was discussed previously. The errors were calculated for the sheet resistance and temperature measurements to be of order 0.1 %. The error bars are not visible on the above plot. For samples grown at 400 and 600 °C, the P_{base} data shows the samples are metallic; whereas, any partial oxygen pressure leads to insulating samples. This shows a complex relationship between the two growth parameters, suggesting several mechanisms are present.

4.2 Discussion

This section will discuss the data in section 4.1 with respect to the growth parameters - P_g and T_g. This aims to give an insight into the mechanisms involved in the pulsed laser deposition, as well as the expected composition of each sample by comparing to the relevant literature. The categories of proposed compositions are shown in figure 11. This analysis allowed the selection of samples for further testing that are likely to display a superconducting ground state to probe the BCS-BEC crossover. Full material characterisation was not in the scope of this project, but this is likely to an aspect of investigation in future projects.
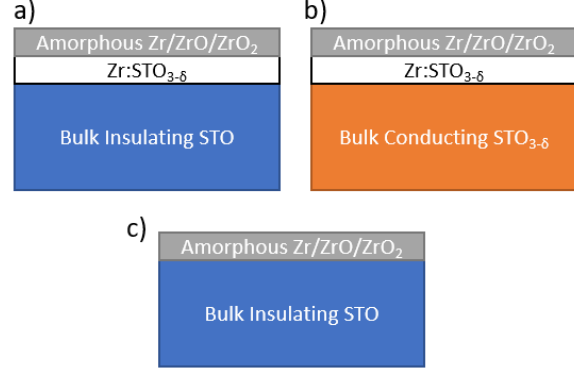

Figure 11: Diagrams showing the cross-section of suggested compositions of samples after pulsed laser deposition. a) represents compositions of samples dominated by thin film conduction. The bulk of the sample is insulating due to a lack of free carriers. The conductive $Zr:STO_{3-\delta}$ layer varies in zirconium content and thickness depending on resistance and RRR. The amorphous layer has unknown composition, possibly consisting of multiple layers. b) shows bulk conducting samples where now carrier concentration in the bulk is sufficient to not suffer from localisation. c) shows an insulating sample with no thin film conduction mechanism present.

Figure 7 has illustrated the effect of increasing growth temperature whilst remaining at base pressure, in this project $P_{base} < 10^{-6}$ mbar. It is suggested here that the dramatic change in sheet resistance (from of order 10^2 to 10^{-2} Ω / sq.) and RRR (from of order 10 to 1000) results from the conduction mechanism moving from a 2DEG thin film contribution to being dominated by a bulk $SrTiO_{3-\delta}$ contribution caused by the creation of bulk oxygen vacancies. This consists of moving from figure 11a) to b). This is an effect that is well-documented for the LAO/STO interface for varying growth pressure [14, 15, 37]; however, there is some disagreement between this project and the literature with regards to pressure measurements. Brinkman et al. [14] found conductive samples for P_g of the order 10^{-3} mbar; whereas, in this project $P_g = 10^{-4}$ mbar generated insulating samples. A possible reason for this could be the accuracy of the pressure measurement. It was found that there was large disagreement between the Chell and Penning

gauges used in this project. The Chell gauge read 0.01 torr (1.3×10^{-2} mbar) for a Penning gauge reading of 10^{-4} mbar. It was assumed the Penning gauge provided greater accuracy at high vacuum; however, the Chell gauge shows greater agreement with the literature. Alternatively, the difference found with the literature could just be a result of the different growth systems. The different target species, geometry of the system, laser energy, and distance between the sample and target will all have an effect. The characteristic shape of the $R(T)$ plots was shown by Brinkman *et al.* to be described by $R_s = a \ln (T/T_{eff}) + bT^2 + cT^5$, where a, b, c are constants and T_{eff} is some crossover temperature. This equation is suggestive of electron-electron scattering in the form of a quadratic term, and electron-phonon scattering in the form of quintic term relevant to higher temperatures. At lower temperatures, a logarithmic term dominates that is suggested to be a result of magnetic scattering in the form of the Kondo effect [14].

With regards to the growth mechanisms present in figure 7, chemical gettering is clearly occurring, creating the thin film zirconium doped SrTiO$_{3-\delta}$ layer. This is confirmed by the $T_g = 25$ °C data, as there is not sufficient thermal energy to create oxygen vacancies by baking out. Therefore, gettering by the uninhibited plume in vacuum is the most likely mechanism to produce $R(T)$ plots of this nature. As the temperature is increased, the gettering effect increases evidenced by the change in resistance and RRR. This shows greater lattice thermal energy enables this mechanism, probably due to a decrease in activation energy for the process to occur. Another effect that will be enabled by lattice thermal energy is the implantation of zirconium as a solid state solution for titanium. As well as possible implantation, there will be the formation of an amorphous layer of Zr/ZrO/ZrO$_2$ above and pure SrTiO$_{3-\delta}$ below, as shown in figure 11. This is similar to the irradiation of STO with Ar$^+$ generating thin film SrTiO$_{3-\delta}$ and an amorphous layer of Ar above [11, 19]. Currently, it is unclear as to the extent at which implantation is evident; however, as shown by Nakagawa *et al.* [38] for the LAO/STO interface, the crossover in an interface is not sharp. This means there will be some zirconium influencing the 2DEG even for an amorphous layer above. The potential of physical sputtering to remove other elements from the lattice is much less likely than generating oxygen vacancies due to the relatively low binding energy and high mobility of oxygen in the lattice [26]. At temperatures including and above 400 °C, the mechanism now dominating is the baking out of oxygen which creates bulk defi-

ciencies leading to a bulk conductor. The literature suggests that the resistance and RRR characteristics seen in this plot are likely to lead to superconductivity for each of these samples [15]; however, the interest in this project is zirconium doped 2DEG superconductors, so bulk samples are not eligible for further investigation.

The data in figure 8 introduces the effect of partial oxygen pressure in the vacuum tank during growth. The suggested conduction mechanism for each sample in this case is a thin film contribution, as shown in figure 11a), supported by [14, 15, 39]. The observed metal to insulator transition for $P_g = 10^{-4}$ mbar is explained by the so-called carrier freeze-out, a previously observed effect for SrTiO$_{3-\delta}$ thin films. This freeze out suggests a low initial 2D carrier density such that the donor energy level is separated from the bottom of the conduction band. As temperature is decreased, the free carriers will become trapped in the lower donor level. These carriers can become re-excited through heating, electric, and magnetic fields. Liu *et al.* found that 2D samples actually showed metal-insulator transitions at a ~ 30 times lower carrier density than bulk samples [40] despite the explanation from Lin *et al.* that the electron mean free path is shorter in lower dimensions [6].

The effect of partial oxygen pressure can reveal insights about the mechanisms involved in this pulsed laser deposition system. Gettering is clearly dependent on partial oxygen pressure as well as growth temperature: it can be seen that gettering is enabled by reducing P_g as more oxygen vacancies are produced leading to lower resistance. This is due to the interaction between the plume and the oxygen present in the tank. Alternatively, the partial oxygen pressure could be filling in vacancies; however, this is unlikely due to the growths being conducted at room temperature. Thus, the kinetic energy of the oxygen will be low. The more likely scenario is the braking of the plume by the oxygen present in the chamber, as shown by Aruta *et al.* [41]. In studying the plasma plume for pulsed laser deposition of LAO and LGO on STO, it was found that the energy of the plume drastically reduced when a critical pressure of 10^{-1} mbar was reached and, at this point, there was no implantation of the target species. At 10^{-2} mbar, plume excitation and oxidation of the target species was observed and implantation of La was limited to 0.6 nm. This shows the implantation of target species is a function of substrate temperature and growth pressure. The growths by Aruta *et al.* were conducted at 800 °C, so the different growth conditions will lead to a different critical pressure. However, there is a large discrep-

ancy between the literature and this project in pressures again. The Penning gauge measurements suggest critical braking is happening at 10^{-4} mbar but the Chell measurements show better agreement with the paper. The fact that the Penning gauge strongly disagrees with all the presented literature could be indicative of an incorrect reading. Alternatively, the differences in the growth systems, mentioned earlier, could be affecting this. Either way, the importance with pressure measurement in this project and future work with this growth equipment is repeatability of growth conditions, so this systematic error is not necessarily a problem.

Figure 9 shows the combination of variation in growth pressure with an introduction of more thermal energy in the substrate. As with figure 8, the conduction mechanism is most likely a thin film contribution, suggested by the resistance values and RRR. Again, it is suggested gettering is the main mechanism for generating charge carriers. Similarly to figure 8, a metal to insulator transition by carrier freeze-out can be seen for the $P_g = 10^{-4}$ mbar sample but at a significantly lower temperature than the $T_g = 25$ °C growths. This, along with the general decrease in resistance across all partial pressures, shows the overall gettering effect has been enabled by increased thermal energy and this dominates over the increase in kinetic energy of the background gas. The effects of increasing the partial oxygen pressure shows roughly the same trend as with the $T_g = 25$ °C growths. However, the critical braking pressure has been moved to a higher value. This could be caused by reduced interaction between the plume and oxygen or, more likely, by the reduced energy barrier to generate oxygen vacancies. The exception to the general trend is the reduction in resistance from $P_g = 6 \times 10^{-6}$ to 1.5×10^{-5} mbar, suggesting an increase in partial pressure leads to more generated oxygen vacancies. This is likely to be a result of experimental error in the growth of samples. The two samples are very close in RRR and resistance, showing the small change in partial oxygen pressure did not have a great effect on growth. Other processes, such as sputtering of Sr and Ti ions and implantation, are more likely to occur at low partial pressures at this growth temperature.

A point noted in figures 8 and 9 is the slight upturn in resistance seen for some samples at low temperatures. This suggests the quantum mechanical effect of weak localisation, a well-documented phenomenon in STO systems [14, 15, 19]. This is an effect observable in disordered systems where electron motion is diffuse, experiencing a series of scattering events when travelling from one point to another. The probability of an electron moving between two points consists of the probabilities of each diffuse path and interference terms between the paths. Due to the increased probability for self-intersecting paths, the interference terms make it such that carriers can be coherently backscattered in the regime where $\tau_e \ll \tau_i$. In this condition, τ_e is the elastic scattering time and τ_i is the inelastic scattering time. Elastic scattering is caused a change in direction but not wavevector and is generally caused by static defects, in this case most likely to be oxygen vacancies. Inelastic scattering results in a change in kinetic energy of the electron, caused by interaction with phonons, photons, and other bosons. Inelastic scattering is largely temperature dependent, at low temperatures the scattering reduces leading to increase τ_i; therefore, at low temperatures $\tau_e \ll \tau_i$ holds true.

Figure 10 gives a summary of the data presented previously now including the samples that were found to be insulating at room temperature. Now, the samples are illustrated by figure 11c), due to a lack of oxygen vacancy generation. Figure 10 illustrates the general decrease in resistance found moving from $T_g = 25$ to 200 °C, which was discussed previously. Additionally, this plot shows a new region for higher growth temperatures where insulating behaviour is now shown. This shows that, for high temperatures, any partial oxygen pressure produces insulating samples. There could be several mechanisms to explain this, one of which being the increased thermal energy of the oxygen atoms. The added energy for oxygen atoms will allow the filling off the bulk deficiencies created through baking out the sample. It could also be the case that the plume interaction with the oxygen is now more significant: the increased energy enables the formation of zirconium oxide which will reduce the ability to getter effectively due to decreased energy of the plume as it deposits. As well as the randomisation of plume velocities for larger partial oxygen pressures. This all contributes to an amorphous layer with no conductive 2DEG below. The amorphous layer on the top of each diagram in figure 11 has currently very little known about it for each samples and it may consist of many layers of varying composition. The glass experimental controls were all insulating apart from one which was subject to carrier freeze out at 250 K. This confirmed that the conduction through the formation of Zr metal on the top layer was not significant in comparison to other mechanisms. There is the possibility of a zirconium oxide layer forming a complex oxide interface with the strontium titanate substrate. This could lead to a more complex contribution to conduction than just oxygen vacancies, as suggested

for the LAO/STO interface [14, 16, 42]. In fact, a recent first principles study has shown altered defect chemistry in the 8.3 % Y_2O_3-ZrO_2/$SrTiO_3$ heterointerface increases ion conductivity [43]. This possibility lies beyond the scope of this project.

The literature suggests there are several samples that are likely to have a superconducting ground state through 2DEG conduction. Additionally, it is suggested that there will be some implantation of zirconium, increasing with growth temperature and reduced growth pressure. Therefore, four samples were chosen for further investigation in the dilution refrigerator for $P_g = P_{base}$ and 6×10^{-6} mbar at $T_g = 25$ and $200°C$. Unfortunately, experimental difficulties meant that one of these samples was not able to be measured.

5   Low Temperature Measurements
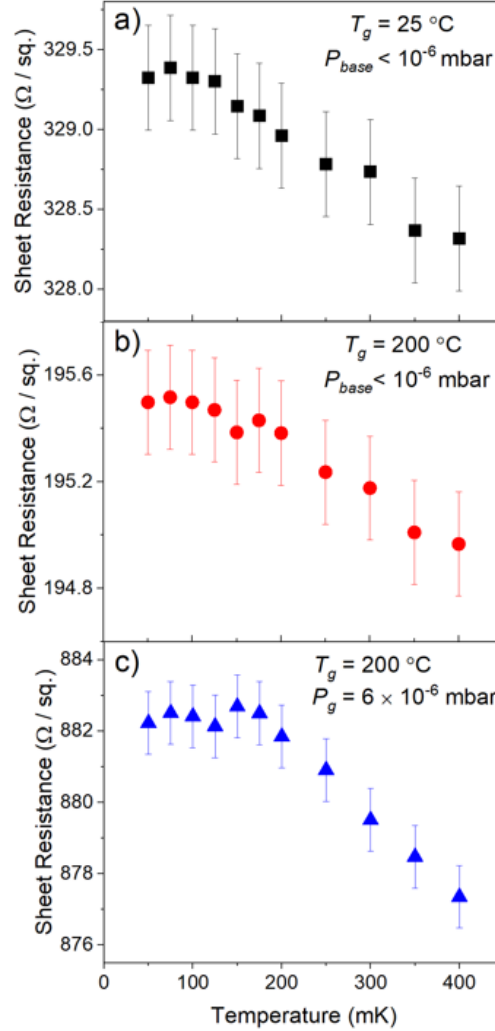
5.1   Results

Figure 12: Plots showing sheet resistance as a function of temperature for three STO samples.

In figure 12, the $R(T)$ data has been extended to between 50 and 400 mK for three STO samples. The data show an increase in resistance for each sample as temperature is reduced up to a certain saturation value. Unfortunately, there was no observed superconducting transition. The error bars on these data are calculated using the equipment errors of 0.1 %.
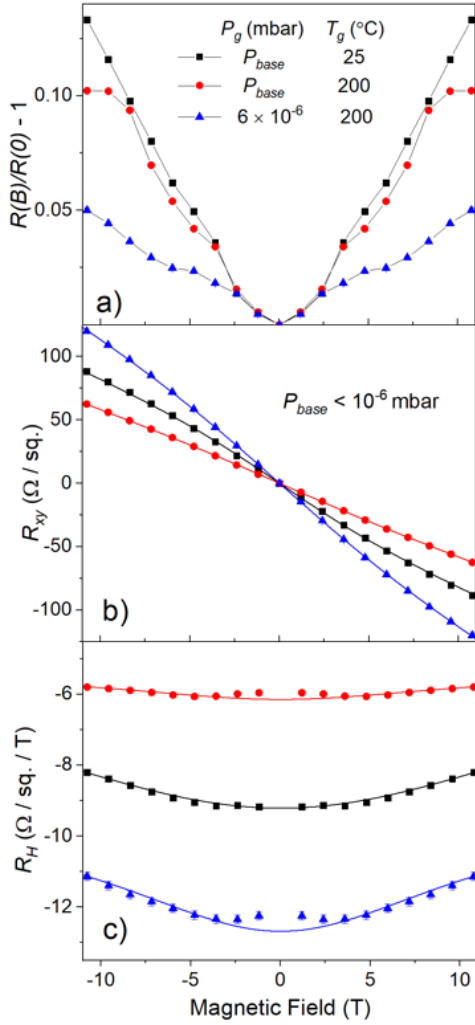
tron mobility (μ_{MR}): $R(B)/R(0) - 1 = \zeta(\mu_{MR}B)^2$ where ζ is of order unity, and R is the magnetoresistance, and B is the magnetic flux density [42]. Values were calculated with a B^2 fit to the low-field data ($|B| < 2.5$ T). Additionally, the Hall electron mobility (μ_H) could be calculated using $\mu_H = 1/eRn$ assuming a simple Drude model, where e is the electronic charge and n is the sheet carrier density calculated as $1/eR_H$. In this case, R_H is the Hall coefficient which is equal to R_{xy}/B [42]. This μ_H was fitted over the same region as μ_{MR} to ensure a fair comparison.

Figure 13: Plots showing perpendicular magnetic field effects on components of resistance for samples at 42 mK. a) Showing the symmeterised magnetoresistance relative to the normal state sheet resistance as a function of applied perpendicular magnetic field for three STO samples. The lines between points are to guide the eye. b) and c) Showing the anti-symmeterised Hall resistance and Hall coefficient as a function of applied perpendicular magnetic field for three STO samples. Each data set has been fitted with the two carrier model.

Figure 13 illustrates the effect of an applied out-of-plane magnetic field ($H_c^\perp$) on the resistivity tensor. The data collected here was by selecting a magnetic field strength, allowing the voltage to stabilise, and then making a measurement. 13a) shows positive magnetoresistance (MR) with applied magnetic field. A known formula was used to calculate the MR elec-
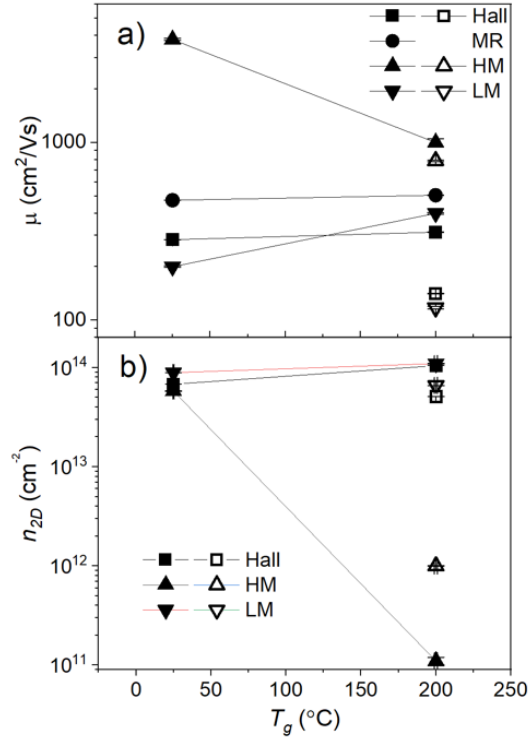
Figure 14: Plots showing the values calculated for the various contributions to the electron mobility and the 2D sheet carrier density. a) and b) Show electron mobility and sheet carrier densities for P_{base} growths (solid symbols) and $P_g = 6 \times 10^{-6}$ mbar growths (open symbols). The lines are to act as guides to the eye.

In figure 13b), the R_{xy} component of the field-dependent resistivity tensor has been plotted for each sample. It shows, as expected, a negative slope confirming the overall charge carrier contribution is electronic. It can be seen that the response is non-linear for each sample, suggesting a two-carrier model is valid. Therefore, equation 7 from appendix section A can be applied to find the contribution from low-

mobility (n_{LM}, μ_{LM}) and high-mobility (n_{HM}, μ_{HM}) carriers present [9]. The quality of this fit was high for each sample, with R^2 values of at least 0.999. In figure 13c), the R_H data shows there is deviation from the model in the low-field region of the plot.

The errors for each component of figure 14 were calculated by taking the error in the resistance measurement to be 0.1 %. The errors on the two carrier model fitting were determined benefitting from the statistical analysis of the two carrier model previously performed by Eguchi *et al.* [44, 45].
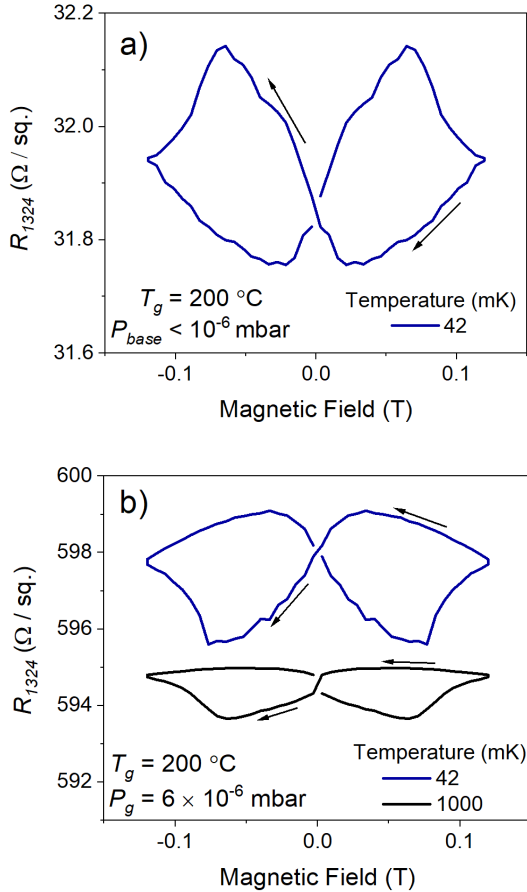

Figure 15: Plots showing hysteresis in one configuration of the van der Pauw magnetoresistance (R_{1324}) for a low-magnetic field sweep. a) Symmeterised data for $T_g = 200$ °C and $P_g = P_{base}$ at 42 mK. b) Symmeterised data for $T_g = 200$ °C and $P_g = 1 \times 10^{-6}$ mbar at 42 and 1000 mK. The arrows on the plots are to show the direction of the magnetoresistance as the field is swept.

To probe the possibility of suppressed superconductivity through trapped flux, a low-field sweep was per-

formed as presented in figure 15. The plot shows no superconducting transition but a clear temperature dependent hysteresis in magnetoresistance. One sample displays a negative magnetoresistance, contrary to the data presented in figure 13a). The data presented is for two of the three samples in one configuration of the van der Pauw method. The third sample did not display this hysteretic behaviour in the configuration tested. Comparing plots in a) and b) reveals that the shape of the hysteresis is inverted between the two.

5.2   Discussion

The key observation presented in figure 12 is the lack of a superconducting transition, instead revealing a slight increase in resistance with decreasing temperature. Several experimental checks were performed to test the lack of a superconducting ground state, the first probing the current (I) vs voltage (V) characteristics of each sample. 2DEG superconductors typically display non-linear IV characteristics below T_c [46], thus any non-linearity may suggest some suppressed superconductivity. The relationship was found to be linear for a range of current sweep values from 0.01 to 10 μA at base temperature of 42 mK. The low-field sweep acted as another check, confirming there was no suppressed superconductivity from trapped flux in the solenoid. The out-of-plane critical field of 2DEG superconductors is of the order 100 mT [46, 47], so it is conceivable that trapped flux in a 12 T solenoid could suppress superconductivity. Additionally, noise and improper grounding could have a contribution; however, there was not sufficient time to explore this. Due to the strong indication from the literature that SrTiO$_{3-\delta}$ with $R(T)$ plots as presented in the previous section will possess a superconducting ground state [14, 15, 39], the lack thereof may be the focus of future investigation.

In terms of the increasing resistance, this can be described by the previously discussed phenomenon of weak localisation. The fractional change of resistance for each sample is small, as shown by the relative size of the error bars to the increase. An alternative suggestion is the Kondo effect, resulting from electron scattering due to magnetic impurities. This mechanism causes the resistance to diverge as $T \to 0$. This effect is suggested to have occurred previously in other STO systems but this is the source of some debate [14, 15, 16]. In fact, in electrolyte gate-controlled undoped SrTiO$_3$ samples, studies suggest this effect was caused by magnetic Ti^{3+} ions, consisting of localised and unpaired electrons and delocalised electrons partially filling the Ti 3d conduction band [48, 49]. In

this case, the possible origin of magnetic cores contributing to scattering is unclear.

The suggestion with regards to the saturation value is a limit in the achievable sample temperature. The sample holder, a bespoke part 3D printed from PLA thermoplastic, was connected to the cold-plate of the fridge with a 280 mm nylon rod. The copper wiring was sufficient to cool by conduction due to the small sample size. Therefore, the plots suggest the thermal lag of the set up limited the temperature to around 100 mK. Nonetheless, the typical superconducting transition temperature of $SrTiO_{3-\delta}$ is greater than this. The jump in resistance in figure 12c) between 125 and 150 mK is most likely experimental error caused by localised heating.

The relationship of magnetoresistance shown in figure 13a) shows a positive increase with applied magnetic field for each sample over a large-scale sweep. This positive MR is a result of the Lorentz force felt by an electron in a magnetic field. This perpendicular field acts by increasing the cyclotron frequency of the **k**-space orbit that the electron is constrained to, leading to an increase in carrier-carrier scattering [50]. MR is also indicative of multi-band conduction where different carriers have different effective mass and mean scattering time, this is further evidenced by the non-linear Hall effect. The high-field MR shows some interesting features in the shape of the plots. This is a result of the error introduced from data collection: due to timing constraints and problems with LabVIEW, this data was taken manually after the voltage was deemed to have stabilised.

Figure 13b) shows the non-linear Hall effect found for each sample. This non-linearity is attributed to a two carrier mechanism comprised of high-mobility and low-mobility carriers. There is more than one possible origin for a two carrier contribution to conduction. One possibility is due different physical locations of charge carriers. The defect structure of the samples will be inhomogeneous with distance from the surface due to the nature of pulsed laser deposition. Close to the surface of the 2DEG, the scattering contribution is likely to be larger leading to a difference in mean scattering times τ. From the scattering times, the difference in carrier mobility can be calculated with $\mu = e\tau/m^*$, where e is the electronic charge and m^* is the electron effective mass. Conversely, the two carrier contribution could be as a result of the complex band structure of strontium titanate shown in figure 16. The schematic shows that bands cross the Fermi level and at low temperatures inter-band scattering is suppressed due to the required momentum change (**k**). Therefore, electrons in each band are

separated and independently contribute to transport with different m^* [16]. Some literature suggests, in the LAO/STO interface, that this two carrier contribution has a critical sheet density at which point the second sub-band is filled [51]. In this case, it is found that greater Hall effect gradient, meaning lower carrier density, leads to more non-linearity. This could be due to an increased thickness of the 2DEG for the $P_{base}, 200$ °C sample. Therefore, the sheet carrier density is greater but the 3D carrier density is less.
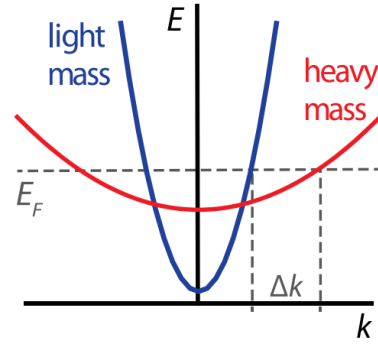

Figure 16: A band structure schematic illustrating the difference between light and heavy mass bands from [16].

Figure 14 shows the contribution to mobility and sheet carrier density for each sample. The Hall effect calculations reveal relatively low mobility and high carrier density in comparison to literature for the LAO/STO interface [16, 42]. The Hall carrier densities can be converted to 3D carrier densities by finding the thickness of thin film conducting layer which can be done in various way. One way is by measuring the in-plane upper critical field $H_{c2}^{\parallel}$ and then the thickness $(d_{Tinkham})$ can be calculated using equation 5 derived with the Tinkham model [22]. An alternative is to use an atomic force microsope (AFM) along the cross section of each sample [52].

$$d_{Tinkham} = \sqrt{\frac{6\Phi_0 H_{c2}^{\perp}}{\pi(H_{c2}^{\parallel})^2}} \tag{5}$$

Due to lack of superconductivity and timing constraints, the thicknesses of samples were not estimated in this project. Therefore, for the purpose of comparison, it is assumed $d_{Tinkham}$ is in the range 5 to 20 nm [12, 15, 22], this corresponds to the 3D carrier densities (n_{3D}) presented in table 1.

| P_g | T_g | Lower Bound | Upper Bound |
(mbar)	(°C)	(cm^{-3})	(cm^{-3})
P_{base}	25	3.4×10^{19}	1.4×10^{20}
P_{base}	200	5.2×10^{19}	2.1×10^{20}
6×10^{-6}	200	2.6×10^{19}	1.0×10^{20}

Table 1: A table showing n_{3D} calculated assuming $d_{Tinkham}$ has a lower bound of 5 nm and an upper bound of 20 nm.

By comparing the results in table 1 with figure 3, the upper bounds are to the far-right of the plot. If the thicknesses are consistent with this upper bound then this could explain the lack of an observed superconducting transition, especially for samples with higher zirconium content. The lower bounds lie around the middle of the plot but it is difficult to draw any conclusions as the zirconium content is unknown. These carrier densities are too great to probe the BCS-BEC crossover, with d_{ee} values of the order of nanometres. They are comparable to normal 2DEG STO systems without zirconium doping [42]. This may suggest that samples with greater room temperature resistance (10^3 to 10^4 Ω / sq.) are required, and the implantation of zirconium is not sufficient to observe the effect witnessed in figure 3. The former requires a reduction in gettering, a route to which could be found from reducing laser energy, frequency, and deposition time. Alternatively, higher quality crystal structure may be required to ensure better conductivity at low carrier densities. If there is a lack of zirconium implantation in the samples, it may be due to T_g being too low, and P_g being too high. However, increasing T_g and lowering P_g will also increase gettering, so a balance must be found. This outcome shows future work should focus on optimising growth parameters to produce the desired sample composition.

It can be seen that there is roughly a 1.6 times increase from the Hall to the MR mobility. The MR mobility could not be extracted in a physically meaningful way for the $T_g = 200$ °C, $P_g = 6 \times 10^{-6}$ mbar data, due to the low-field magnetoresistance shape. This variation could be due to anisotropy in wavevector, generating a direction depending scattering time. Alternatively, this may be due to the quality of the low-field MR fit. The mobility and sheet carrier density data for the two carrier model clearly shows separate contributions for high and low-mobility carriers. Each sample appears to be dominated by low-mobility carriers, with a fractional contribution from high-mobility carriers. Except for P_{base}, 25 °C, which shows a similar contribution for high and low-mobility carriers. However, there is a large variation in mobility and, as described in appendix section A, this can introduce an error into the estimation of n_{total} leading to an error in the fit. The low-field deviation from the model in figure 13c) has several possible explanations. It could be due to to physical mechanisms in the samples being more complex than a simple two carrier model. Alternatively, it could be due to some experimental error in the low-field limit but this is unlikely as the deviation varies between samples.

In figure 15, the low-field sweep reveals temperature dependent hysteresis in the MR of two STO samples. As the arrows on the plots show, one sample demonstrates a negative response and the other a positive response. The negative response reveals an effect hidden by the resolution of the high-field sweep. There are several explanations for this negative MR. One explanation is due to increasing carrier density as the magnetic field increases, as originally proposed for carbons [53]. This is due to the electrons being confined to Landau levels in the presence of a perpendicular magnetic field, the density of states of these levels is proportional to the magnetic field. However, at fields as low as used in this project, this is an unlikely cause. An alternative explanation is through a weak localisation effect that has been described previously. The effect of an applied magnetic field is to reverse the resistance increase observed at low temperatures. The field suppresses the constructive interference of backscattered pairs by introducing phase shifts [19]. The negative MR could be due to the alignment of electrons and ions with the field leading to reduced spin scattering. If spins are anti-parallel, there are more available states to scatter into. Therefore, the probability of scattering is greater and the resistance is larger. Negative MR can be indicative of magnetic scattering, due to a ferromagnetic or paramagnetic moment [14]. It is difficult to distinguish between localisation and magnetic effects as they scale similarly with magnetic fields. These effects are only present for one sample, with the lowest sheet carrier density of the three. The positive MR for each sample at large fields shows that carrier-carrier scattering dominates in this region.

The shape of this hysteresis is similar to previously observed at the LAO/STO interface [14, 15, 54]. These papers claim this hysteresis effect is indicative of ferromagnetic domain formation. These domains change polarity above a certain coercive field and this generates a residual signal when crossing zero field. However, this is said not to completely explain

the observed effect due to the suppression at zero field when it is expected to occur after the sign of the field changes. The combination of this, low-temperature resistance upturn, and negative MR is suggested to require magnetic scattering centres as magnetic moments and give further evidence for the Kondo effect. Doubts have been cast on this conclusion due to the field sweep rate of 30 mT/s, which is fast in comparison to this project where the rate was 1 mT/s. It is possible that the hysteresis observed in the LAO/STO interface is due a temperature effect from eddy current heating. With regards to this project, it could allow the explanation of the inverse relationship between 15a) and b). It was found that R_{1324} increased with temperature for the sample in a) and decreased for the sample in b). However, this eddy current heating explanation is hindered by the fact that hysteresis was only observed for two samples. The lack of hysteretic behaviour was seen in the sample that showed the lowest resistance in one configuration of the van der Pauw resistance but not the lowest sheet resistance. Equation 6 represents the power dissipation P per unit mass due to a peak magnetic field B_p swept at frequency f for a thin sheet sample with thickness d, density D, and sheet resistance R_s [55]. Using this equation and assuming the samples are of the same form factor, the increase in power from eddy current heating should be inversely proportional to the sheet resistance. This is inconsistent with the observation of a lack of hysteresis in a sample with significantly lower sheet resistance than that of the sample in figure 15b). Figure 12 shows that there should be a comparable effect on resistance due to an increase in temperature. An identical shape MR hysteresis was observed in the superconducting semiconductor GeTe [56]. The lack of eddy current heating is confirmed by starting a 1.4 mT/s sweep in a superconducting state and recovering the superconducting state at the end of the sweep, showing the sample has not been heated during the sweep. The mechanism underlying the hysteresis is said to be specific to Rashba spin superconductors resulting from non-equilibrium behaviour.

$$P = \frac{\pi^2 B_p^2 df^2}{6R_s D} \tag{6}$$

This hysteresis effect has previously been seen in Co-doped ZnO thin films [50] and topologically insulating thin films that have been magnetically doped [57]. Both of these studies suggest that the cause of the hysteresis is characteristic of spin-dependent scattering by local magnetic ordering for ferromagnetic metals. However, these papers all see negative MR for large field sweeps which is not observed here. The inverse of this butterfly hysteresis, seen in figure 15a), was observed in thin film Fe_3O_4 grown on an Si substrate followed by a large field positive MR [58]. This unique MR was intensively studied and the proposed mechanism was a spin-filter effect. This is due to the strong negative spin polarisation of Fe_3O_4 leading to conduction mechanism being dominated by spin-down electrons in an applied magnetic field. The carriers injected from attached electrodes are not polarised, so the spin-up electrons (50 % of injected carriers) experience much larger scattering at the interface between electrodes and thin film. Only spin down electrons can find a path through the thin film, leading to an increase in resistance. It is suggested that the hysteresis is a result of the method of magnetisation of the thin film. This leads to the tentative conclusion that the samples in this project contain some form of magnetic scattering. The two samples displaying hysteresis are for growth temperatures of 200 °C and the other sample was grown at 25 °C. At the higher temperature, zirconium implantation will be more likely, suggesting that this observed effect may be a result of zirconium content; however, such a mechanism is currently unclear.

6 Conclusion

The project has endeavoured to utilise the remarkable properties of strontium titanate, that allow superconductivity to be observed to such low carrier densities, in order to probe to BCS-BEC crossover. Epitaxial thin films of zirconium doped strontium titanate were grown by pulsed laser deposition, resulting in oxygen gettering to release electrons to become available as carriers. Initial $R(T)$ measurements allowed the selection of samples that were likely to display superconducting ground states with a 2DEG conduction mechanism. These samples underwent further testing in a dilution refrigerator and measurements were taken for low temperature resistance, magnetoresistance, and the Hall effect. The reason for a lack of superconductivity is unknown but suggested explanations could be noise and grounding problems, or high carrier densities. These high carrier densities lead to d_{ee} of the order of nanometres, placing the sample firmly on the BCS side of the crossover. The non-linear Hall effect and magnetoresistance measurements allowed the calculation of Hall and MR carrier density and mobility, and the application of a two carrier model. An interesting butterfly and inverse butterfly MR was observed in a low-field sweep at 42 mK for samples grown at $T_g = 200$ °C. This may suggest the presence of magnetic order and spin scattering due to the implantation of zirconium.

The experimental procedure of STO pulsed laser deposition of zirconium developed in this project is still in the early stages and needs refining. What is required is a study of growth parameters to minimise the carrier density and improve zirconium implantation whilst remaining in a metallic state and not suffering low temperature carrier freeze out. This will allow the desired samples to be produced that can offer a route to the BCS-BEC crossover. Thus providing supporting or contradictory evidence to the application of the work of Hulm *et al.* [7] to a 2DEG. However, this work will be futile unless the resulting samples are superconducting. The further exploration of the lack of this is a necessary future step. Other suggested ways of extending the work in this project are as follows: determining the thickness of the conducting 2DEG layer using methods described previously; and further dilution refrigerator measurements to further explore the MR hysteresis and confirm the lack of eddy current heating.

References

[1] J Bardeen, L N Cooper, and J R Schrieffer. "Theory of Superconductivity". In: *Phys. Rev.* 108 (1957), p. 5.

[2] J Ruhman and P A Lee. "Superconductivity at very low density: The case of strontium titanate". In: *Physical Review B* 94 (2016).

[3] Y Nakagawa et al. "Gate-controlled low carrier density superconductors: Toward the two-dimensional BCS-BEC crossover". In: *Phys. Rev. B* 98 (6 2018), p. 064512.

[4] J F Schooley, W R Hosler, and M L Cohen. "Superconductivity in Semiconducting SrTiO$_3$". In: *Phys. Rev. Lett.* 12 (1964), p. 474.

[5] A Spinelli et al. "Electronic transport in doped SrTiO$_3$: Conduction mechanisms and potential applications". In: *Phys. Rev. B* 81.15, 155110 (2010), p. 155110.

[6] X Lin et al. "Fermi Surface of the Most Dilute Superconductor". In: *Phys. Rev. X* 3 (2 2013), p. 021002.

[7] J K Hulm et al. "Low Carrier Concentration Superconductors". In: *Proc. lOth International Conference on Low Temperature Physics*. Vol. IIA. VINITI, Moscow, Russia, 2009, p. 86.

[8] D M Eagles. "Superconductivity at Very Low Carrier Concentrations and Indications of a Charged Bose Gas in SrTi$_{0.97}$Zr$_{0.03}$O$_3$". In: *Solid State Com.* 60 (1986), p. 6.

[9] Z Chen et al. "Supporting Information: Dual-Gate Modulation of Carrier Density and Disorder in an Oxide Two-Dimensional Electron System". In: *Nano Lett.* 16 (10 2016), pp. 6130–6136.

[10] M Kim et al. "Fermi Surface and Superconductivity in Low-Density High-Mobility δ-Doped SrTiO$_3$". In: *Phys. Rev. Lett.* 107 (2011), p. 106801.

[11] D Kan et al. "Blue-light emission at room temperature from Ar+-irradiated SrTiO$_3$". In: *Nature Materials* 4 (2005), pp. 816–819.

[12] Y Kozuka et al. "Two-dimensional normal-state quantum oscillations in a superconducting heterostructure". In: *Nature* 462 (2009), pp. 487–90.

[13] D G Schlom and J Mannhart. "Oxide electronics: Interface takes charge over Si". In: *Nature materials* 10 3 (2011), pp. 168–9.

[14] A Brinkman et al. "Magnetic effects at the interface between non-magnetic oxides". In: *Nature materials* 6 (Aug. 2007), pp. 493–6.

[15] M Huijben et al. "Structure-property relation of SrTiO3/LaAlO3 interfaces". In: *Advanced Materials* 21 (Mar. 2009), pp. 1665–1677.

[16] F Gunkel et al. "Defect-control of conventional and anomalous electron transport at complex oxide interfaces". In: *Phys. Rev. X* 6 (2016). ISSN: 2160-3308.

[17] G Cheng et al. "Electron pairing without superconductivity". In: *Nature* 521 (2015), pp. 196–9.

[18] G Cheng et al. "Tunable Electron-Electron Interactions in LaAlO3/SrTiO3 Nanostructures". In: *Phys. Rev. X* 6 (2016).

[19] J H Ngai et al. "Electric field tuned crossover from classical to weakly localized quantum transport in electron doped $SrTiO_3$". In: *Phys. Rev.* B81 (2010), 241307(R).

[20] L N Cooper. "Bound Electron Pairs in a Degenerate Fermi Gas". In: *Phys. Rev.* 104 (1956), p. 1189.

[21] A B Migdal. "Interactions between Electrons and Lattice Vibrations in a Normal Metal". In: *Soviet Phys. JETP* 34 (7) (1958), p. 996.

[22] M Kim et al. "Intrinsic spin-orbit coupling in superconducting δ-doped $SrTiO_3$ heterostructures". In: *Phys. Rev. B* 86 (8 2012), p. 085121.

[23] M M Parish. "The BCS-BEC Crossover". In: *Quantum Gas Experiments: Exploring Many-Body States.* World Scientific Publishing Co. Pte. Ltd., 2015, pp. 179–197.

[24] M G Ries et al. "Observation of pair condensation in the Quasi-2D BEC-BCS Crossover". In: *Phys. Rev. Lett.* 114 (2015), p. 230401.

[25] H Suzuki et al. "Superconductivity in Single-Crystalline Sr1-xLaxTiO3". In: *Journal of the Physical Society of Japan* 65 (May 1996), p. 1529.

[26] A G H Smith. "Structural and Defect Properties of Strontium Titanate". PhD thesis. University College London, 2011.

[27] Hanno H Weitering and Judy Z Wu. "Superconductivity: how the unconventional became the new norm". In: *Superconductor Science and Technology* 30.4 (2017), p. 040301.

[28] J F Schooley et al. "Dependence of the Superconducting Transition Temperature on Carrier Concentration in Semiconducting $SrTiO_3$". In: *Phys. Rev. Lett.* 14 (1965), pp. 305–307.

[29] M S Alkathy, A Joseph, and K C J Raju. "Dielectric Properties of Zr substituted Barium Strontium Titanate". In: *Materials Today: Proceedings* 3.6 (2016), pp. 2321–2328.

[30] K Behnia. "On mobility of electrons in a shallow Fermi sea over a rough seafloor". In: *Journal of Physics: Condensed Matter* 27.37 (2015), p. 375501.

[31] R M Park et al. *Manual on the Use of Thermocouples in Temperature Measurement.* 4th Edn. ASTM International, 2003.

[32] L J van der Pauw. "A method of measuring specific resistivity and Hall effect of discsof arbitrary shape". In: *Phillips Research Reports* 13.19 (1958).

[33] G Teleberg and G Batey. *Principles of dilution refrigeration: A brief technology guide.* v19. Tubney Woods, Abingdon, UK: Oxford Instruments Nanoscience, 2015.

[34] E Thuneberg. Aug. 2003. URL: http://ltl.tkk.fi/research/theory/mixture.html (visited on 04/04/2019).

[35] P Hofmann. *Solid State Physics, An Introduction.* 2nd Edn. Weinheim, Germany: Wiley VCH, 2015.

[36] C Thomas. "Strained HgTe/CdTe topological insulators, toward spintronic applications". PhD thesis. Universite Grenoble Alpes, 2016.

[37] A Kalabukhov et al. "Effect of Oxygen Vacancies in the $SrTiO_3$ Substrate on the Electrical Properties of the $LaAlO_3$/$SrTiO_3$ Interface". In: *Phys. Rev. B* 75 (2007).

[38] N Nakagawa, H Y. Hwang, and D A. Muller. "Why some interfaces cannot be sharp". In: *Nature Materials* 5 (2006), pp. 204–209.

[39] Y Chen. "A high-mobility two-dimensional electron gas at the spinel/perovskite interface of γ-Al_2O_3/$SrTiO_3$". In: *Nature Communications* 4 (2013), p. 1371.

[40] Z Q Liu et al. "Metal-Insulator Transition in $SrTiO_{3-x}$ Thin Films Induced by Frozen-Out Carriers". In: *Phys. Rev. Lett.* 107 (14 2011), p. 146802.

[41] C Aruta et al. "Pulsed laser deposition of SrTiO$_3$ / LaGaO$_3$ and SrTiO$_3$ / LaAlO$_3$: Plasma plume effects". In: *Appl. Phys. Lett.* 97 (2010), p. 252105.

[42] C Bell et al. "Thickness dependence of the mobility at the LaAlO3/SrTiO3 interface". In: *Appl. Phys. Lett.* 94 (June 2009), pp. 222111–222111.

[43] A Kushima and B Yildiz. "Role of Lattice Strain and Defect Chemistry on the Oxygen Vacancy Migration at the (8.3 % Y2O3-ZrO2) / SrTiO3 Hetero-Interface: A First Principles Study". In: *ECS Transactions* 25 (2009).

[44] G Eguchi et al. "Precise determination of two-carrier transport properties in the topological insulator TlBiSe$_2$". In: *Phys. Rev. B* 91 (2015).

[45] G Eguchi and S Paschen. "Robust scheme for magnetotransport analysis in topological insulators". In: *Phys. Rev. B* 99 (16 2019), p. 165128.

[46] Y L Han and et al. "Two-dimensional superconductivity at (110) LaAlO3/SrTiO3 interfaces". In: *Appl. Phys. Lett.* 105 (10 2014), p. 192603.

[47] N Reyren et al. "Anisotropy of the superconducting transport properties of the LaAlO3/SrTiO3 interface". In: *Appl. Phys. Lett.* 94 (2009), p. 112506.

[48] M Li et al. "Role of Percolation in the Conductance of Electrolyte-Gated SrTiO$_3$". In: *Phys. Rev. Lett.* 109 (2012), p. 196803.

[49] M Lee et al. "Electrolyte Gate-Controlled Kondo Effect in SrTiO$_3$". In: *Phys. Rev. Lett.* 107 (2011), p. 256601.

[50] P Stamenov et al. "Magnetoresistance of Co-doped ZnO thin films". In: *Journ. of Appl. Phys.* 99 (May 2006), pp. 08M124–08M124.

[51] A Joshua et al. "A universal critical density underlying the physics of electrons at the LaAlO3/SrTiO3 interface". In: *Nature communications* 3 (2012), p. 1129.

[52] M Basletic et al. "Mapping the Spatial Distribution of Charge Carriers in LaAlO3/SrTiO3 Heterostructures". In: *Nature materials* 7 (2008), pp. 621–5.

[53] A A Bright. "Negative magnetoresistance of pregraphitic carbons". In: *Phys. Rev. B* 20 (12 1979), pp. 5142–5149.

[54] D A Dikin et al. "Coexistence of Superconductivity and Ferromagnetism in Two Dimensions". In: *Phys. Rev. Lett.* 107 (5 2011), p. 056802.

[55] F Fiorillo. *Measurement and characterization of magnetic materials.* Cambridge, Massachusetts, USA: Elsevier Academic Press, 2004, p. 31.

[56] V Narayan et al. "Long-lived non-equilibrium superconductivity in a non-centrosymmetric Rashba semiconductor". In: *Preprint: arXiv:1902.04675* (Feb. 2019).

[57] Z Zhang et al. "Electrically tuned magnetic order and magnetoresistance in a topological insulator". In: *Nature communications* 5 (2014), p. 4915.

[58] E Liu et al. "Inverse Magnetoresistance in textured Fe$_3$O$_4$ Film". In: *Journal of Alloys and Compounds* 649 (2015).

Appendices

A   Two Carrier Model

$$R_{xy} = -\frac{1}{e} \frac{\left(\dfrac{n_{LM}\mu_{LM}^2}{1+\mu_{LM}^2 B^2} + \dfrac{n_{HM}\mu_{HM}^2}{1+\mu_{HM}^2 B^2}\right)B}{\left(\dfrac{n_{LM}\mu_{LM}}{1+\mu_{LM}^2 B^2} + \dfrac{n_{HM}\mu_{HM}}{1+\mu_{HM}^2 B^2}\right)^2 + \left(\dfrac{n_{LM}\mu_{LM}^2}{1+\mu_{LM}^2 B^2} + \dfrac{n_{HM}\mu_{HM}^2}{1+\mu_{HM}^2 B^2}\right)^2 B^2} \tag{7}$$

In this equation, n_{LM} and μ_{LM} show the mobility and carrier density for the low-mobility carriers, n_{HM} and μ_{HM} for high-mobility carriers. This equation was solved for each R_{xy} data set using the scipy.optimize least-squares minimisation method in python subject to the constraints that $n_{LM} + n_{HM} = n_{total}$ and $1/R_{xx}(B=0) = e(n_{LM}\mu_{LM} + n_{HM}\mu_{HM})$. Here, n_{total} was calculated using the saturating value of dR_{xy}/dB for large fields, as this value tends to $1/en_{total}$ for $B \to \infty$. The accuracy of this approximation depends on the relation between μ_{LM} and μ_{HM}. If the difference is large, then a large magnetic field is required to capture the total electron density and this can lead to some experimental error [9].

B Declaration

I hereby assert that I own exclusive copyright in the item named below. I give permission to the University of Bristol Library to add this item to its stock and to make it available for consultation in the library, and for inter-library lending for use in another library. It may be copied in full or in part for any bona fide library or research worked, on the understanding that users are made aware of their obligations under copyright legislation, i.e. that no quotation and no information derived from it may be published without the authors prior consent.

Author	Oliver Joseph Sellers
Title	Pulsed Laser Deposition of Low Density Superconductors
Date of submission	29/04/2019

Signed: O J Sellers

Full name: Oliver Joseph Sellers

Date: 29/04/2019

This project is the property of the University of Bristol Library and may only be used with due regard to the rights of the author. Bibliographical references may be noted, but no part may be copied for use or quotation in any published work without the prior permission of the author. In addition, due acknowledgement for any use must be made.